ATMOSPHERIC SCIENCE

Opening the window to the Southern Ocean: The role of jet dynamics

Andreas Klocker[1,2,3]*

The surface waters of the Southern Ocean act as a control valve through which climatically important tracers such as heat, freshwater, and CO_2 are transferred between the atmosphere and the ocean. The process that transports these tracers through the surface mixed layer into the ocean interior is known as ocean ventilation. Changes in ocean ventilation are thought to be important for both rapid transitions of the ocean's global overturning circulation during the last deglaciation and the uptake and storage of excess heat and CO_2 as a consequence of anthropogenic climate change. I show how the interaction between Southern Ocean jets, topographic features, and ocean stratification can lead to rapid changes in Southern Ocean ventilation as a function of wind stress. For increasing winds, this interaction leads from a state in which tracers are confined to the surface mixed layer to a state in which tracers fill the ocean interior. For sufficiently high winds, the jet dynamics abruptly change, allowing the tracer to ventilate a water mass known as Antarctic Intermediate Water in the mid-depth Southern Ocean. Abrupt changes in Antarctic Intermediate Water ventilation have played a major role in rapid climate transitions in Earth's past, and combined with the results presented here, this would suggest that jet dynamics could play a prominent role in contributing to, or even triggering, rapid transitions of the global climate system.

INTRODUCTION

The ocean is the global climate system's second largest reservoir of heat and carbon dioxide (CO_2) behind the solid Earth. Because of the correlation between global temperature and atmospheric CO_2 concentrations over glacial cycles, the time scales involved, and the ocean's capability to store large amounts of CO_2, it is thought that the ocean is a major player behind these changes (*1*). Most of the ocean below a depth of 1 km interacts with the atmosphere through less than 4% of the ocean's surface area, mostly at high latitudes (*2*). These high-latitude areas, particularly the Southern Ocean, are therefore crucial in controlling the exchange of CO_2 between the atmosphere and the deep ocean. Numerous proxy data obtained from sediment cores, used to reconstruct past patterns of ocean circulation, confirm the important role of the Southern Ocean (*3*, *4*). In particular, the ventilation of a water mass known as Antarctic Intermediate Water (AAIW) is of global significance. AAIW is formed by fresh Antarctic Surface Waters (AASW) ventilating the mid-depth Southern Ocean (*5*), leading to the redistribution of heat, freshwater, and nutrients throughout the global ocean (*6*, *7*). AAIW is a significant sink of anthropogenic CO_2 (*8*) and is recognized as being pivotal in explaining rapid transitions observed in Earth's past climate (*9*). Both observational (*10*) and model studies (*11*, *12*) show a possible link between abrupt changes in the ventilation of AAIW and the collapse of North Atlantic Deep Water formation, pointing toward a crucial role of AAIW ventilation in contributing to, or even triggering, abrupt reorganizations of the global meridional overturning circulation (MOC).

Because of the rotation of Earth, persistent westerly winds over the Southern Ocean push surface waters to the north, leading to the steepening of isopycnals and subsequently the upwelling of carbon and nutrient-rich deep waters as part of the Southern Ocean MOC (*13*). Once these deep waters reach the ocean surface, they are able to exchange properties with the atmosphere before they re-ventilate the ocean interior. The resulting carbon budget is a delicate balance between these ventilation pathways (*14*). From a physical perspective, the balance between the outgassing of CO_2 from the upwelling of natural carbon-rich deep waters and the drawdown of atmospheric CO_2 by the ventilation process determines whether the Southern Ocean acts as a sink or source of CO_2 to the atmosphere (*15*, *16*). If the biological perspective is taken into account, this balance is also responsible for the availability of nutrients at the ocean surface, with consequences for the export of carbon into the ocean interior due to the sinking of biological matter (*17*). The net role of the Southern Ocean as a source or sink of CO_2 is therefore a combination of both physical and biological processes (*3*, *4*).

Fueled by observation-based evidence of rapid climate transitions in Earth's past, and the uncertainty of the ocean's heat and CO_2 uptake in future climates, substantial effort has gone into understanding how these processes are likely to change under varying wind forcing (*15*, *18*, *19*), buoyancy forcing (*15*, *20*), and sea ice cover (*21*). Most of this effort has focused on the wind-induced overturning by the Southern Ocean MOC. It has been shown that the upwelling of deep waters, although partially compensated by mesoscale eddies, increases continuously for an increase in wind stress (*22*). With winds predicted to increase under anthropogenic forcing (*23*), this would lead to enhanced outgassing of CO_2 in the future, opposing anthropogenic carbon uptake (*24*), although these results remain controversial (*25*). While substantial progress in understanding this upwelling process has been made, very little is known about the processes that lead to the re-ventilation of these water masses. This is particularly the case for the ventilation of AAIW, for which many processes have been suggested as possible candidates, such as convection driven by air-sea fluxes, Ekman transport, eddy and turbulent mixing, and mixing at the base of the mixed layer, but no conclusion has been reached (*26*).

This study sheds some light on this problem by using a high-resolution numerical model of the Indian sector of the Southern Ocean to elucidate on the processes relevant to Southern Ocean ventilation.

[1]Institute for Marine and Antarctic Studies, University of Tasmania, Hobart, Tasmania, Australia. [2]Australian Research Council Centre of Excellence for Climate System Science, University of Tasmania, Hobart, Tasmania, Australia. [3]Antarctic Climate and Ecosystems Cooperative Research Centre, University of Tasmania, Hobart, Tasmania, Australia.
*Corresponding author. Email: andreas.klocker@utas.edu.au

Using the topographically steered jet north of the Kerguelen Plateau (KP) as an example, I show how changes in wind stress affect jet dynamics and their interaction with topographic features and stratification. The sensitivity of jet dynamics to wind stress leads to changes in Southern Ocean ventilation, which are an order of magnitude larger than would be expected from changes in the Southern Ocean MOC alone. Once the wind stress is increased beyond a certain threshold, the jet dynamics abruptly change, allowing for the ventilation of AAIW. Since the jet dynamics discussed here depend on small-scale turbulent processes, it will be a tremendous challenge to represent these jet dynamics, and their effect on Southern Ocean ventilation, in models used for simulations of past and future climates. Nevertheless, it is only once we understand these dynamics that we can confidently predict possible rapid transitions in a future climate.

RESULTS

Model simulations show rapid change in ocean ventilation

The time- and depth-mean circulation in an eddy-resolving ocean model (Materials and Methods) of the Indian sector of the Southern Ocean is shown in Fig. 1A. The prominent topographic features in this region are the KP and the SEIR, both of which develop strong jets along their northern boundaries due to the interaction of the Southern Ocean's background mean flow with topography. The model experiment shown represents "modern" conditions, with the wind and buoyancy forcing being annually and zonally averaged values from the year 2005. Six perturbation experiments were run in which the zonal component of the wind stress was varied, while all other forcing was kept constant (in the following, modern wind stress is denoted by τ, and perturbation experiments range from $0.5*\tau$ to $2*\tau$; Fig. 1B). In each experiment, a passive tracer, intended to represent a chemical species, such as CO_2, undergoing atmosphere-ocean exchange processes but ignoring biological and chemical interaction, is introduced homogeneously at the ocean surface for 10 years after model equilibration. This passive tracer is restored with a 2-hour time scale, approximating an infinite tracer reservoir in the surface mixed layer (SML). Results below are shown after 5 years of tracer ventilation since, after this time, the limited domain of this model configuration affects results (Materials and Methods).

The first striking result of these model experiments is evident from Fig. 1C, which shows changes of the maximum of the Southern Ocean MOC (blue line; Materials and Methods), and tracer concentrations in the ocean interior (integrated between depths of 500 and 1500 m) after 5 years (red line; Materials and Methods), as a function of changes in wind stress. The black line represents a 1:1 relationship between wind stress and ventilation changes. This figure shows that Southern Ocean ventilation, assuming an infinite tracer reservoir in the SML, is much more sensitive to changes in wind stress than the maximum in Southern Ocean MOC, which is the metric currently used to understand the role of Southern Ocean ventilation in past and future climates. For the perturbation experiments

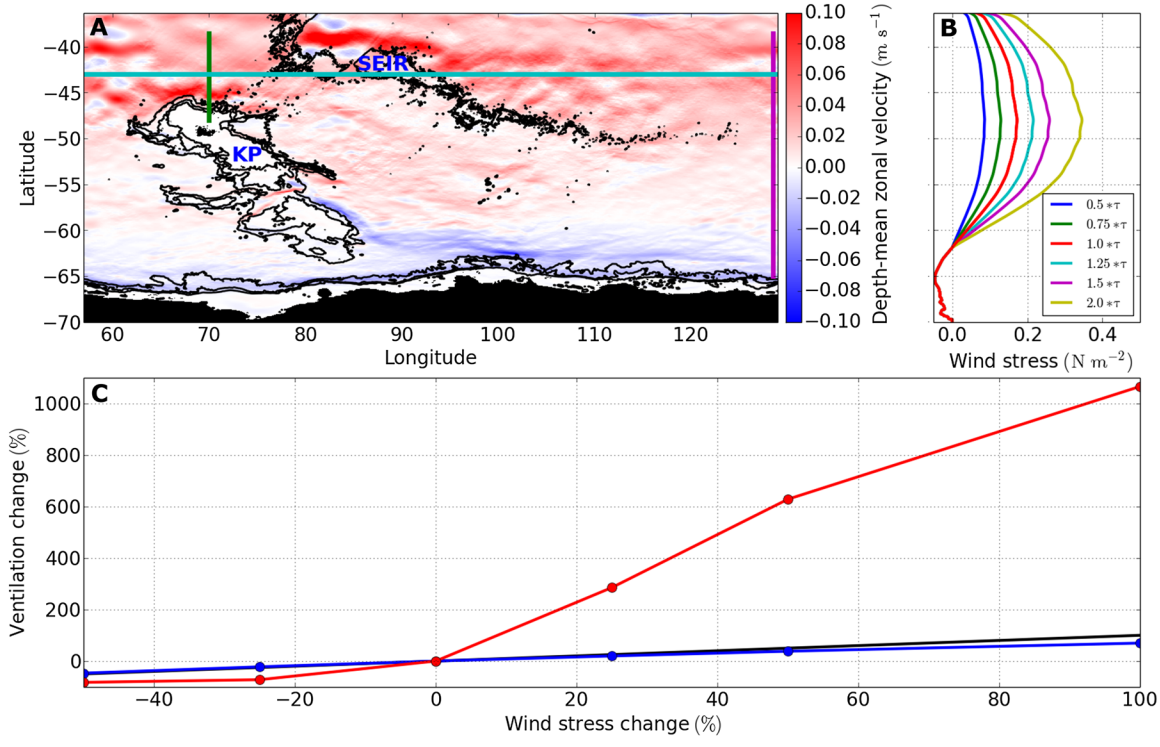

Fig. 1. Numerical simulation of the Southern Ocean ventilation. (**A**) Time- and depth-mean zonal velocities for the modern wind stress (color) and ocean depth (contours). Both the KP and the South East Indian Ridge (SEIR) are marked. Colored lines show locations of vertical transects shown in Figs.3 and 4. (**B**) Wind stress (N m^{-2}) of the six perturbation experiments (the red line represents modern conditions). Only the westerly components of the wind stress are changed. (**C**) Changes in Southern Ocean ventilation as a function of changes in wind stress, where zero marks the annual and zonal average winds of 2005. The blue line shows changes in Southern Ocean overturning, the red line shows changes in tracer uptake integrated between water depths of 500 and 1500 m, and the black line shows the 1:1 line, that is, where wind changes equal ventilation changes. Circular markers show the different perturbation experiments.

with a wind stress below modern values, changes in tracer ventilation are about twice as large as changes in the maximum of the Southern Ocean MOC, whereas for the perturbation experiments with a wind stress above modern values, changes in tracer ventilation are about one order of magnitude larger than changes in the maximum of the Southern Ocean MOC. As will be shown below, both the high sensitivity of Southern Ocean ventilation to wind stress and the change of behavior at modern wind stress values are closely related to changes in jet dynamics and their interaction with topography and stratification.

The second striking result is evident from Fig. 2, which shows the geographic location at which the tracer ventilates the ocean interior. Snapshots of tracer concentrations at a depth of 200 m are shown for two perturbation experiments—for a wind stress of τ, 8 months after the tracer is introduced (Fig. 2A), and for a wind stress of 2*τ, 4 months after the tracer is first introduced (Fig. 2B). These snapshots focus on the time when the tracer first ventilates the ocean interior and before the tracer is advected beyond the ventilation region. Note that because of the differences in ventilation mechanism, both times of snapshots and color scales in Fig. 2 (A and B) are different. These examples highlight the two different states of tracer ventilation, closely linked to two different dynamical states of the jet north of the KP (referred to as the Kerguelen jet in the following). For the perturbation experiment with a wind stress of τ (Fig. 2A), tracer ventilation predominantly occurs in filaments downstream of the Kerguelen jet in a region commonly referred to as oceanic storm track, with storm tracks being regions of anomalously high eddy kinetic energy (EKE) downstream of topographic features caused by the instability of jets (*27*). On the other hand, for the perturbation experiment with a wind stress of 2*τ (Fig. 2B), tracer ventilation occurs along the Kerguelen jet. Both states of tracer ventilation have very different consequences for Southern Ocean ventilation.

The role of the Kerguelen jet in these two states of tracer ventilation becomes even more evident by examining the time-mean tracer forcing at the ocean surface for the perturbation experiments with a wind stress of τ (Fig. 3A) and 2*τ (Fig. 3B) and the time-mean vertical tracer advection at a depth of 200 m, where the depth is chosen to visualize the tracer being advected across the base of the SML, for the same perturbation experiments (Fig. 3, C and D, respectively). The perturbation experiment with a wind stress of 2*τ shows enhanced values for the tracer forcing at the ocean surface, which is consistent with an increased tracer ventilation by the Kerguelen jet, reducing the tracer concentration at the ocean surface and subsequently increasing the tracer forcing that restores the tracer concentration at the ocean surface (Materials and Methods). The enhanced values of tracer forcing at the northern boundary are due to currents coming out of the northern sponge layer where the tracer concentration is restored to zero and hence are a numerical artifact. The time-mean vertical tracer advection in the perturbation experiment for a wind stress of 2*τ also shows much larger values than the perturbation experiment for a wind stress of τ, with changes again occurring along the core of the Kerguelen jet. From this figure, it is also evident that the dominant length scales of upward and downward advection, of the order of 100 km, point toward tracer ventilation being a consequence of the Kerguelen jet interacting with standing mesoscale features. Note though that this long-term mean will remove the footprint of small-scale eddies simply due to the chaotic and short-lived nature of these eddies. These small-scale eddies are crucial for the upper ocean vertical transport and are mostly due to mixed layer instabilities and frontogenesis that can be enhanced in an energetic mesoscale eddy strain field relevant to jets. In the

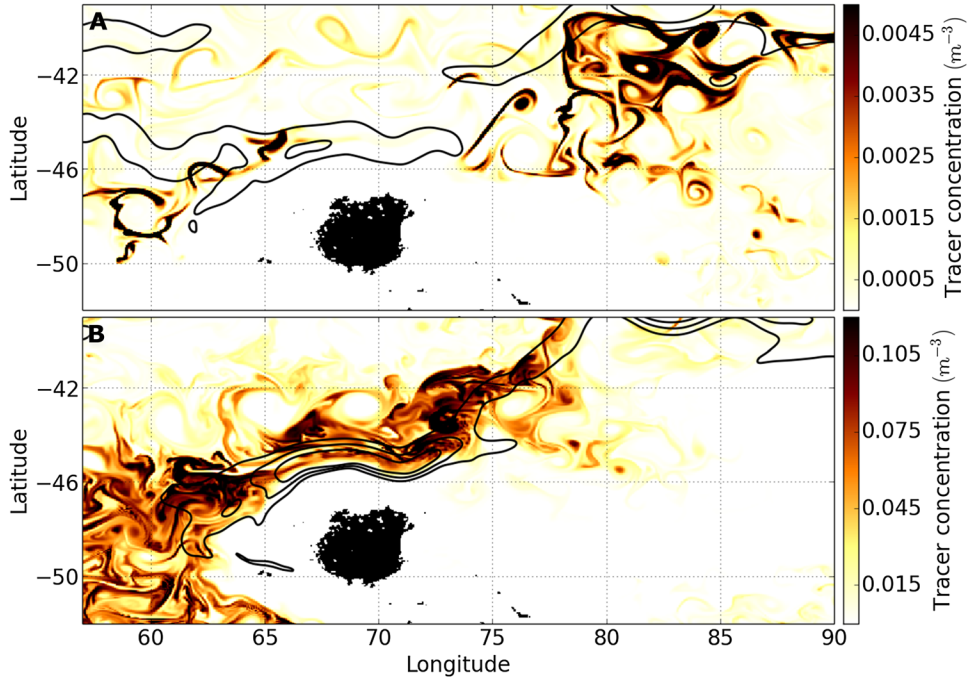

Fig. 2. Tracer ventilation as a function of jet dynamics. Tracer concentration at a depth of 200 m for a wind stress of (**A**) τ, 8 months after the tracer is first introduced, and a wind stress of (**B**) 2*τ, 4 months after the tracer is introduced. Black contours show time-mean velocities at 200 m to highlight the position of the Kerguelen jet. Note the different color scales.

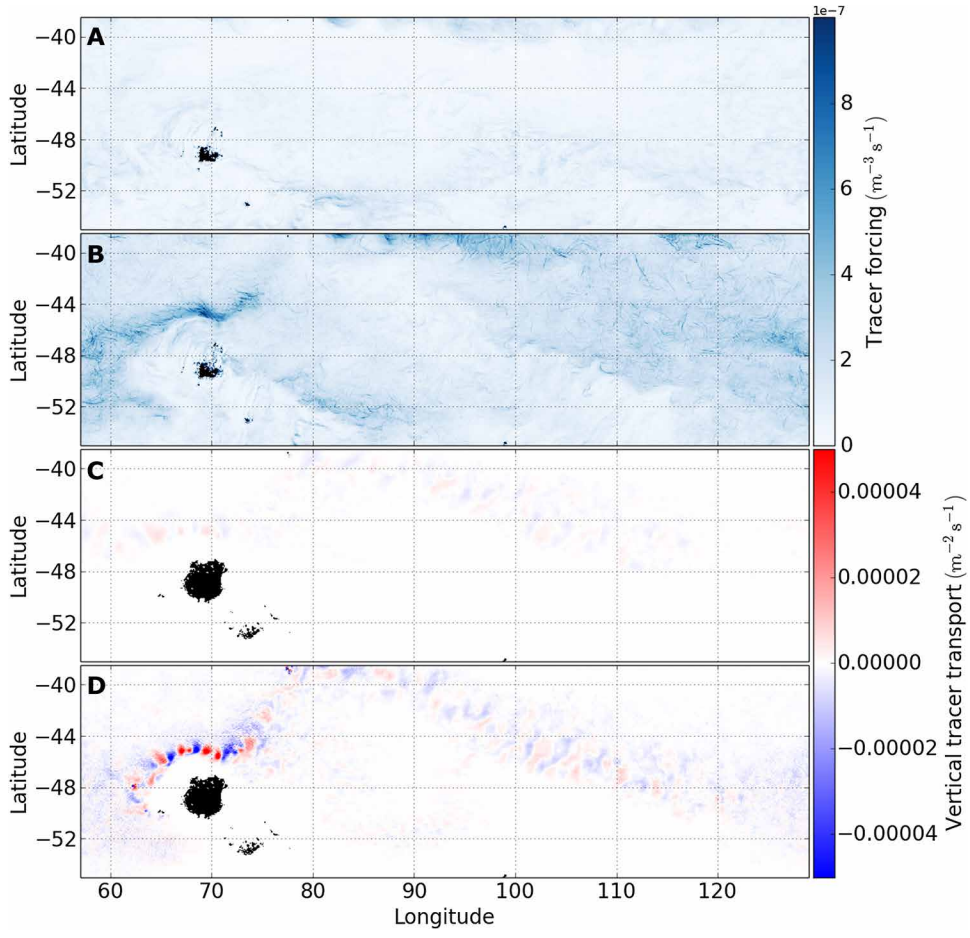

Fig. 3. Location of tracer ventilation. Time-mean tracer forcing at the ocean surface for the perturbation experiment with a wind stress of (**A**) τ and a wind stress of (**B**) 2*τ. Time-mean vertical tracer advection at a depth 200 m for the perturbation experiment with a wind stress of (**C**) τ and a wind stress of (**D**) 2*τ.

following, the perturbation experiments with wind stresses of 0.5*τ, τ, and 2*τ will be used to further highlight the differences in tracer ventilation and jet dynamics, with the focus being on the Kerguelen jet.

With tracer concentrations being visualized as colored dye on a $\log_{10}$ scale, Fig. 4 shows the extent to which the passive tracer has ventilated the ocean interior after 5 years. Vertical sections of tracer concentrations are shown in Fig. 4 (A to C) for the cyan transect in Fig. 1A and in Fig. 4 (D to F) for the purple transect in Fig. 1A. The cyan transect is chosen to be north of the ventilation region, and the purple transect is chosen to be downstream of the ventilation region, both to highlight tracer concentrations in the ocean interior rather than the ventilation region. Black contours in Fig. 4 (A to F) represent salinity, with AAIW being defined by the salinity minimum evident between depths of approximately 500 and 1500 m. For a wind stress of 0.5*τ, the tracer is confined to the SML and hence there is no ventilation of the ocean interior (Fig. 4, A and D). For a wind stress of τ, the tracer is ventilated into the top ~500 m of the water column, with tracer concentrations decreasing monotonically with depth (Fig. 4, B and E). For a wind stress of 2*τ, the tracer is ventilated across the base of the SML into AAIW, with a vertical separation between elevated tracer concentrations in the SML and AAIW (Fig. 4, C and F). These results would suggest that tracer ventilation in storm track leads to deep SMLs, while tracer ventilation along the jet leads to tracer ventilation across the base of the SML into AAIW.

Tracer ventilation intimately linked to jet dynamics

The different states of tracer ventilation are intimately linked to changes in jet dynamics, best explained using time-mean hydrographic sections across the Kerguelen jet, as shown in Fig. 5 for the green transect in Fig. 1A. The time-mean ocean properties in Fig. 5 are zonal velocity (Fig. 5, A to C), stratification (shown as buoyancy frequency; Fig. 5, D to F), and salinity (Fig. 5, G to I) for wind stresses of 0.5*τ (Fig. 5, A, D, and G), τ (Fig. 5, B, E, and H), and 2*τ (Fig. 5, C, F, and I). The black feature in these panels is the northern edge of the KP, white contours mark isopycnal surfaces, and the approximate location of the bottom of the SML is shown by the green line. Figure 5 (J to L) shows a horizontal section of stratification at a depth of 120 m (which is approximately the depth of the SML) for the same perturbation experiments. The red patch in Fig. 5H highlights a region of convection. Additional insight is gained from the transient behavior of the jet, shown on a Hovmöller diagram of zonal velocities at the ocean surface for wind stresses of 0.5*τ (Fig. 5M), τ (Fig. 5N), and 2*τ (Fig. 5O). The abrupt change in jet dynamics occurs at a critical point between wind stresses of τ and 2*τ (at approximately a wind stress of 1.25*τ, which will become

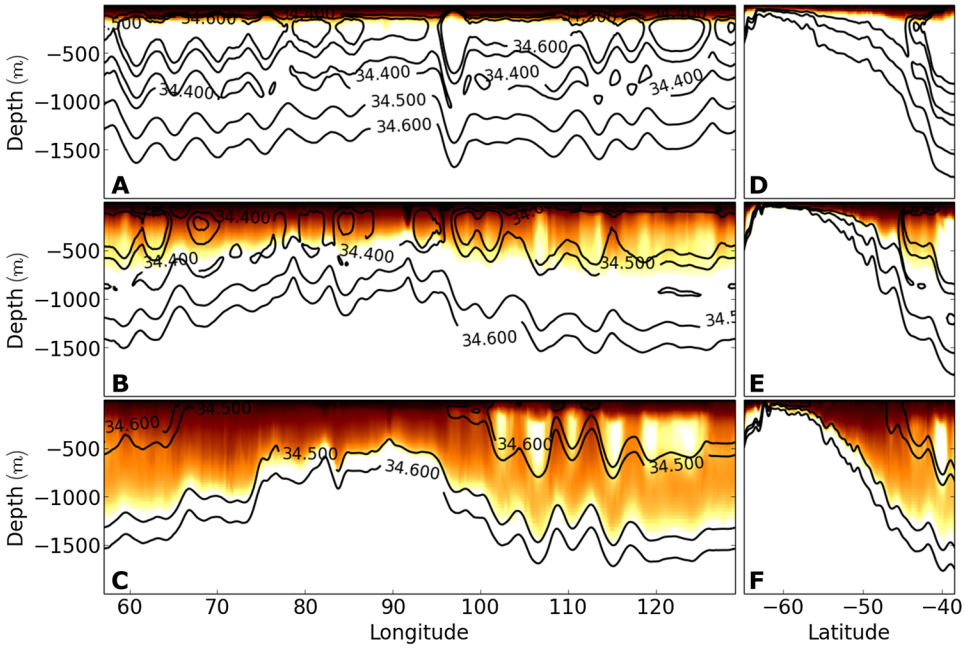

Fig. 4. Tracer ventilation as a function of wind forcing. Vertical section along a latitude of 43°S (cyan transect in Fig.1A) showing tracer concentration (color; on a $\log_{10}$ scale) and salinity (psu, practical salinity unit) (contours) for the perturbation experiment with wind stresses of (**A**) 0.5*τ, (**B**) τ, and (**C**) 2*τ. Vertical section along a longitude of 129°E (magenta transect in Fig.1A) showing tracer concentration (color; on a $\log_{10}$ scale) and salinity (contours) for the perturbation experiment with wind stresses of (**D**) 0.5*τ, (**E**) τ, and (**F**) 2*τ.

evident below). Beyond the critical point, the Kerguelen jet suddenly accelerates, westward jets appear at its flanks (Fig. 5, A, D, and G), and, as seen in the Hovmöller diagram, the Kerguelen jet becomes more steady, locked in latitude, and smaller length scales appear (Fig. 5, M to O). While an increase in wind stress from 0.5*τ to τ leads to a decrease in stratification across the base of the SML across the Kerguelen jet (Fig. 5, B and E), it is only when the wind stress increases to 2*τ that convection across the base of the SML occurs, resulting in the ventilation of fresh (that is, low salinity) surface waters, known as AASW, into AAIW (Fig. 5, C, F, and I), consistent with the ventilation of the passive tracer shown in Fig. 4.

This change in jet dynamics—ignoring their effect on ventilation for a moment—can be understood in more detail from Fig. 6. Shown are time and zonal means, averaged between 66°E and 70°E, of vertical profiles of zonal velocities in the jet's core (Fig. 6A, solid lines) and its northern flank (Fig. 6A, dashed lines), depth-mean zonal velocities (Fig. 6B), depth-mean EKE (Fig. 6C), and the cross-jet potential vorticity gradient (Fig. 6D). The potential vorticity gradient is a metric that is closely associated with the stability properties of a jet. A zero crossing in the potential vorticity gradient is associated with the necessary condition for the instability of the jet. The potential vorticity gradient used here is defined as $\beta^* = \beta - U_{yy}$ and hence includes a contribution from Earth's rotation ($\beta = f_y$, where f is the Coriolis parameter and y is latitude) and the meridional shear of the jet's depth-mean flow (U_{yy}), and is a proxy for the jet's barotropic stability properties (*28*). In particular, the jet can become barotropically unstable when the stabilizing effect due to Earth's rotation is counteracted by the horizontal shear of the jet. Note that the topographic influence on the potential vorticity gradient is ignored here since it is not clear at which length scales topography affects jet dynamics.

The change in jet dynamics shown in Figs. 5 and 6 can be interpreted as follows. For a wind stress of 0.5*τ, the jet core has near-zero bottom velocities (Fig. 6A, blue line) and its potential vorticity gradient is positive everywhere across the jet (Fig. 6C, blue line). For this state, an increase in wind stress to τ leads to an increase in the jet's vertical shear (Fig. 6A) and, consequently, an increase in its baroclinic instability with an associated increase in EKE (Fig. 6C). At the critical point, the potential vorticity gradient approaches zero at its southern flank (Fig. 6D), with a zero crossing of the potential vorticity gradient being the necessary condition for the barotropic instability of the jet (*29*). Once the wind stress further increases, the jet abruptly reorganizes its structure to equilibrate its eddy instabilities through modification of its mean structure by eddy fluxes (*30*). As a consequence, the eastward jet core significantly accelerates while its flanks develop two westward jets, leading to a large increase in the jet's lateral shear (Figs. 5, G and L, and 6, A and B). This jet structure is now associated with a large positive potential vorticity gradient across the jet's core and negative potential vorticity gradients across both of its flanks (Fig. 6D). Beyond the critical point, a further increase in wind stress results in the acceleration of the jet core's depth-mean velocities and, subsequently, a further increase in the jet's lateral shear while keeping its vertical shear near constant (Fig. 6, A and B). At the critical point, the jet dynamics therefore abruptly change from that of a baroclinic jet, in which the jet's vertical shear increases as the jet is accelerated, to that of a barotropic jet, in which the jet's lateral shear increases as the jet is accelerated. This strong lateral shear is known to be able to suppress baroclinic instability, a process known as the barotropic governor (*31*), which explains why this jet can sustain such steep isopycnals without becoming unstable. The effects of jet dynamics on baroclinic instability and, hence, EKE can be used to find the critical point at

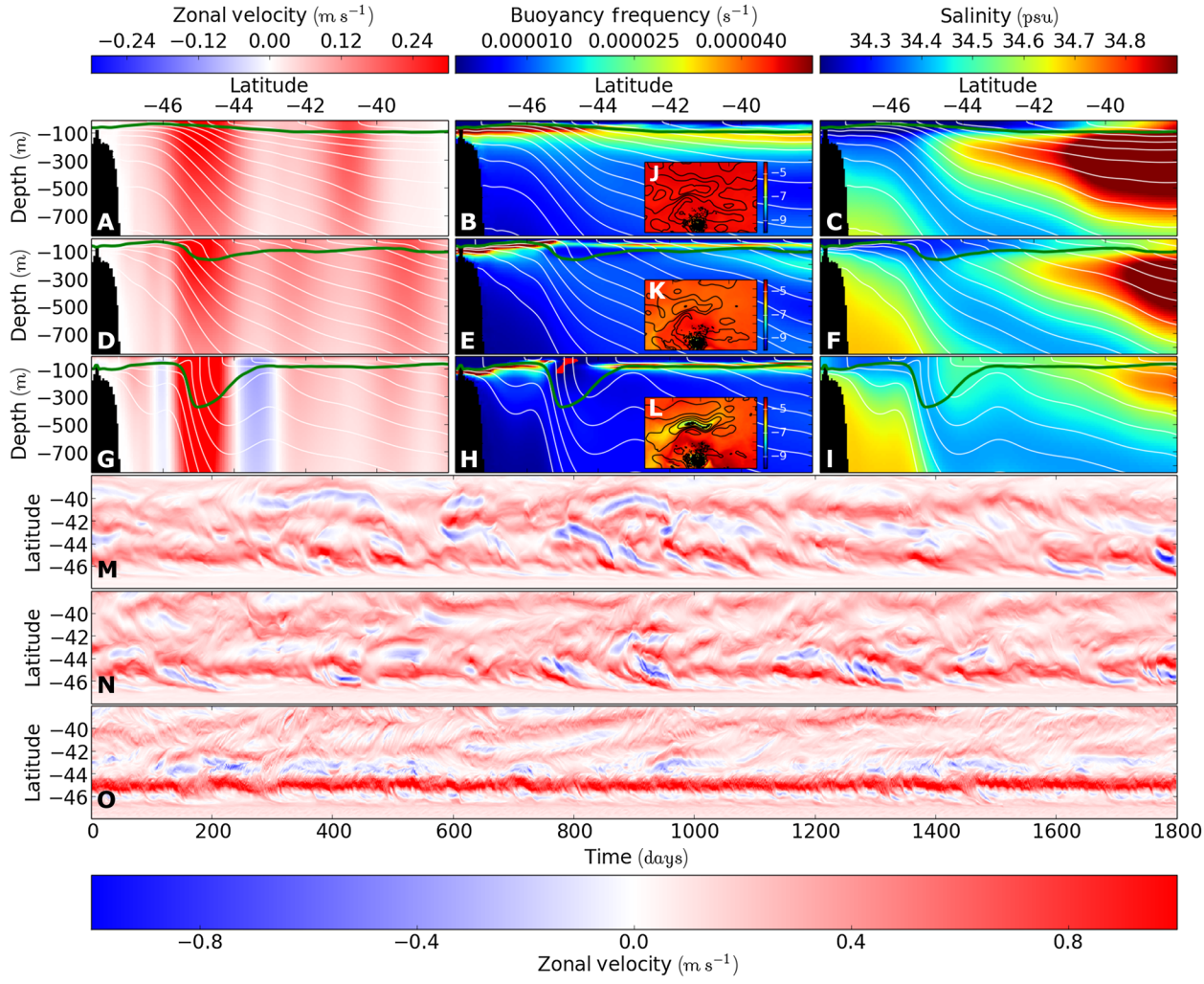

Fig. 5. Hydrographic sections across the Kerguelen jet. Colors show vertical sections along the green transect in Fig.1A of time-mean (**A**, **D**, and **G**) zonal velocity (meters per second), (**B**, **E**, and **H**) buoyancy frequency (per second), and (**C**, **F**, and **I**) salinity (psu), for the perturbation experiments with wind stresses of (A to C) 0.5*τ, (D to F) τ, and (G to I) 2*τ. White contours are time-mean isopycnals, and the green line is the time-mean mixed layer depth. The black feature is the northern slope of the KP. The red patch in (H) marks a region of time-mean convection. Horizontal sections of time-mean buoyancy frequency (per second) on a $\log_{10}$ scale at a depth of 120 m, chosen to represent the depth of the base of the SML, for the perturbation experiments with wind stresses of (**J**) 0.5*τ, (**K**) τ, and (**L**) 2*τ. Hovmöller diagrams of zonal surface velocities along the green transect in Fig.1 for (**M**) 0.5*τ, (**N**) τ, and (**O**) 2*τ.

which jet dynamics abruptly change. From Fig. 5C, it is apparent that EKE adjacent to the jet increases from a wind stress of 0.5*τ to 1.25*τ, reaches a maximum of 1.25*τ, and then decreases with further increases in wind stress. This is particularly evident in the region where the shear between the eastward jet core and its westward jets at its flanks becomes largest due to the barotropic governor increasingly suppressing baroclinic instability. For the Kerguelen jet, the critical point occurs for a wind stress increase of 25%.

In the Southern Ocean, strong westerly winds prevail and hence blow into the direction of the jets, a scenario usually referred to as "down-front winds" (*32*). These down-front winds lead to Ekman advection of buoyancy across the jet. Depending on the lateral gradients of buoyancy and momentum across the jet, the Ekman advection of buoyancy can lead to convection across the base of the SML (*32*). As evident from vertical sections of stratification across the Kerguelen jet (Fig. 5, B, E, and H), increasing winds erode the stratification across the base of the SML across all perturbation experiments, but it is only beyond the critical point, where the jet changes from baroclinic to barotropic, that this reduction in stratification is sufficient to lead to convection across the base of the SML [Fig. 5, B, E, and H; note that the mixed layer depth in the jet (~400 m in the case of 2*τ) is much deeper than the boundary layer parameterized by KPP (K-profile parameterization) for the same region (~100 m in the case of 2*τ) and hence is not a numerical artifact due to the choice of this parameterization scheme (Materials and Methods)]. This convection allows the passive tracer (Fig. 4, C and F) and AASW (Fig. 5I) to ventilate AAIW along the jet. As evident from Fig. 5 (J to L), which shows a horizontal section of stratification at the base of the mixed layer at a depth of 120 m, convection across the base of the SML is confined to the core of the jet, that is, regions where lateral gradients of buoyancy and momentum are largest. These results therefore point toward the possibility of the abrupt reorganization from a baroclinic to a barotropic jet and the associated increase in the lateral gradients of buoyancy and momentum, which is a prerequisite for the ventilation of AAIW along the jet.

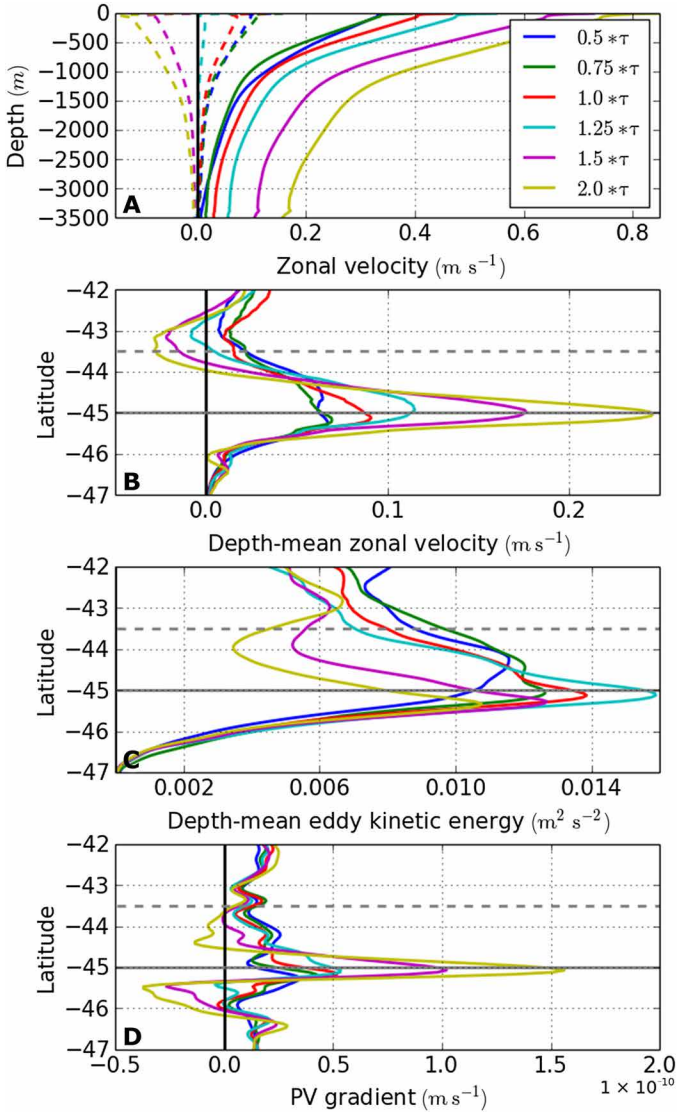

Fig. 6. Dynamics of the Kerguelen jet. Jet properties are time- and zonal-mean values calculated between 66°E and 70°E. (**A**) Solid lines represent vertical profiles of zonal velocities in the core [at 45°S; solid gray line in (B) to (D)] of the eastward jet. Dashed lines represent vertical profiles of zonal velocities at the northern flank [at 43°S; dashed gray line in (B) to (D)] of the jet. (**B**) Depth-mean zonal velocities across the jet. (**C**) Depth mean EKE across the jet. (**D**) Smoothed potential vorticity (PV) gradient $\beta^* = \beta - U_{yy}$, where β is the meridional gradient of the Coriolis force and U_{yy} is the meridional shear of the depth-mean zonal velocity. Colors represent the different wind perturbation experiments shown in Fig.1B.

The role of jet dynamics in Southern Ocean ventilation can be summarized as follows. Because of the interaction of the Southern Ocean's background mean flow with topography, strong jets appear adjacent to this topography, such as the Kerguelen jet discussed here. For the example of the Kerguelen jet, an increase in winds of up to 1.25*τ leads to an increase in the jet's vertical shear, which is associated with an increase in EKE due to baroclinic instability in both the jet and the associated storm track. The consequence of this increase in storm track intensity is a change from no tracer ventilation (0.5*τ) to the tracer being ventilated into a deep SML (0.75*τ to 1.25*τ). Once the wind stress increases beyond the critical point at 1.25*τ, the jet abruptly changes its structure to a barotropic jet with westward jets at its flanks, increasing its lateral shear and hence suppressing baroclinic instability due to an effect known as the barotropic governor. Because of the emerging barotropic governor, a further increase in winds leads to a decrease in EKE and increasingly steep isopycnal surfaces. This abrupt increase in cross-jet gradients of buoyancy and momentum, combined with down-front winds, leads to convection across the base of the SML. This convection across the base of the mixed layer, combined with the steep isopycnal surfaces across the jet, leads to the ventilation of AAIW along the jet.

While the model experiments shown here resolve mesoscale turbulence with length scales of the order of 10 to 100 km and Rossby numbers of $R_o = \zeta/f << 1$ (where $\zeta = v_x - u_y$ is the relative vorticity and f is the planetary vorticity), these model experiments barely resolve submesoscale turbulence with length scales of the order of 1 to 10 km and Rossby numbers of $R_o = O(1)$. Nevertheless, it is the submesoscale turbulence, which is associated with strong vertical velocities, that is thought to dominate tracer ventilation (*33*). An insight into how the dynamics presented here could affect submesoscale turbulence and hence tracer ventilation can be gained from snapshots of Rossby numbers for the different perturbation experiments (Fig. 7). For a wind stress of 0.5*τ, the Rossby number $R_o << 1$ (Fig. 7A), and no tracer ventilation occurs. For a wind stress of τ, the Rossby number R_o increases predominantly in the storm track downstream of topography (Fig. 7B), consistent with tracer ventilation occurring in this region. For a wind stress of 2*τ, the cross-jet gradients of buoyancy and momentum abruptly increase. This increase in cross-jet buoyancy gradient energizes submesoscale turbulence (*33*), which is consistent with Rossby numbers abruptly increasing to $R_o = O(1)$ adjacent to the Kerguelen jet (Fig. 7C). If submesoscale turbulence were resolved, then the ventilation of the tracer would very likely substantially increase in regions of $R_o = O(1)$.

Model results agree with observations of jets and ventilation

While observations related to the dynamics of Southern Ocean jets and their effect on tracer ventilation are sparse, the few observations that exist are consistent with the dynamics proposed here. Using observational data sets, it has been shown that Southern Ocean ventilation is a very localized process, associated with topographic features (*34*). This has also been confirmed using observationally based estimates of anthropogenic carbon concentrations to show the localized nature of anthropogenic CO_2 ventilation (*35*). More recent work has used biogeochemical autonomous floats (BGCArgo) to detect intermittent ventilation events in oceanic storm tracks (*36*). All these observational studies agree with the jet dynamics in the case of a baroclinic jet, with ventilation occurring in storm tracks. For the ventilation of AAIW, in the case of a barotropic jet, observations become even more sparse. Most of the AAIW ventilation under current climate forcing occurs in Drake Passage, where the Southern Ocean jet known as the polar front (PF) is pushed through the narrow gap between South America and Antarctica. Observations of the PF in this region show both zero crossings of the cross-jet potential vorticity gradient and bottom velocities of the order of 0.04 to 0.05 m s^{-1} (*37*), similar to the barotropic state of the jet discussed here, that is, the state for which AAIW ventilation occurs. In 1998, an interference between El Nino–Southern Oscillation and the Southern Annular Mode led to an anomalous wind forcing with winds in the region of AAIW ventilation being directed in an up-front

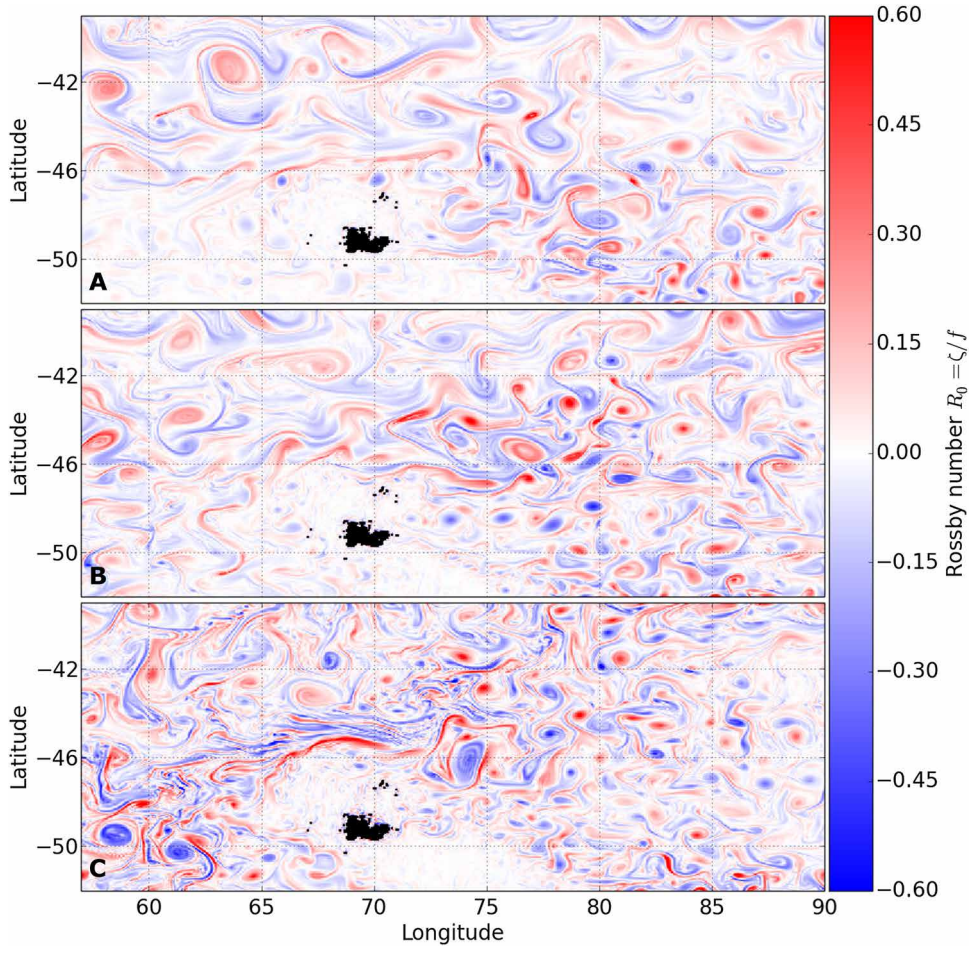

Fig. 7. The dependence of Rossby numbers on wind stress. Rossby numbers $R_o = \zeta/f$, where $\zeta = v_x - u_y$ is the relative vorticity and f is the planetary vorticity, at the ocean surface for (**A**) 0.5*τ, (**B**) τ, and (**C**) 2*τ.

direction rather than the usual down-front direction. A time series of physical and biogeochemical properties between 1969 and 2005, produced from transects across Drake Passage, shows that in 1998/1999, AAIW suddenly warmed, salinified, and de-oxygenated (*5*). These observations suggest an interruption of AAIW ventilation for 1 to 2 years following this anomalous wind forcing, pointing toward the crucial role of down-front winds in ventilating the ocean interior. Nevertheless, to test whether this anomaly in AAIW ventilation can be explained by the jet dynamics introduced here, it would be necessary to run multiple perturbation experiments of the circulation in Drake Passage. These experiments would be technically very challenging and computationally expensive since the topography of Drake Passage prevents the use of a simple re-entrant model configuration, as done in this study, and hence it would be necessary to simulate the full Southern Ocean.

DISCUSSION

While a plethora of observation-based evidence points toward the existence of rapid climate transitions in Earth's past, and it is generally accepted that these are closely linked to Southern Ocean dynamics, the processes relevant to contributing to, or triggering, these rapid climate transitions have remained elusive. Here, I show, using the jet north of the KP as an example, how the dynamics of Southern Ocean jets and their interaction with topographic features and ocean stratification can lead to rapid changes in Southern Ocean ventilation. For a small increase in wind stress, these jet dynamics lead from a state where the tracer is confined to the SML to a state where the tracer is ventilated into the ocean interior. Once a certain threshold in wind stress is passed, jet dynamics abruptly change, allowing for the ventilation of fresh AASW into AAIW. These dynamics could lead to a rapid change in Southern Ocean surface stratification, the transport of heat, freshwater, and nutrients at intermediate depths into the global ocean, and could potentially have crucial impacts for the Atlantic MOC. On the basis of observation-based evidence of past ocean circulation, all of these changes are thought to have played a crucial role in rapid climate transitions in Earth's past (*28*, *38*, *39*). In addition to consequences on the surface and mid-depth ocean, changes in freshwater forcing in the shallow Southern Ocean can lead to changes in the global deep ocean stratification (*40*) and hence modify the efficiency of the deep global ocean as a carbon trap (*41*).

There are two main reasons why it is only now that the important role of jets in Southern Ocean ventilation has emerged. First, it

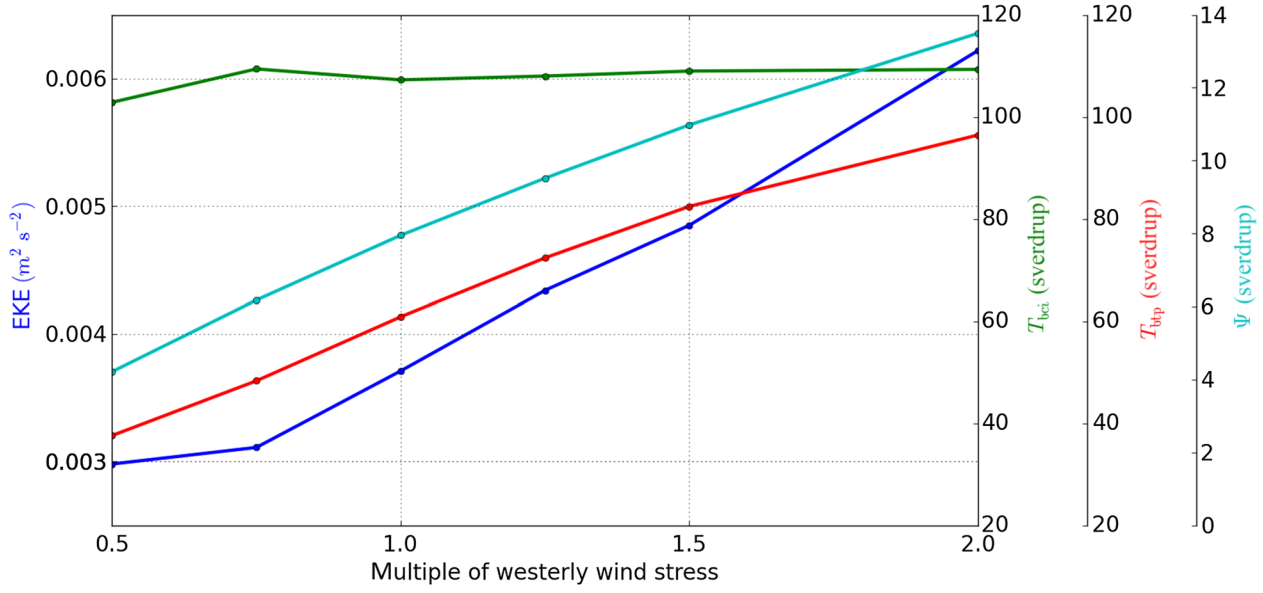

Fig. 8. Properties of equilibrated perturbation experiments. Equilibrated mean EKE (blue line), baroclinic transport (T_{bci}; green line), barotropic transport (T_{btp}; red line), and maximum MOC (Ψ; cyan line) are shown for all the perturbation experiments. Transports are given in units of Sverdrup, where 1 Sverdrup = 10^6 m^3 s^{-1}.

is only over the past few years that it has become evident that nonzonal dynamics are essential to understand the Southern Ocean's Antarctic Circumpolar Current, such as, for example, its equilibration (*42*) and the localized nature of observed CO_2 ventilation (*35*). Much of the previous literature on ocean ventilation has focused on the role of the Southern Ocean MOC, which is generally assumed to be a residual between the wind-driven Ekman overturning circulation and an eddy overturning circulation driven by eddy buoyancy fluxes, with eddy momentum fluxes (also known as Reynolds stresses) assumed negligible. Nevertheless, to understand the localized jet dynamics presented here, it is necessary to take into account eddy momentum fluxes, which are closely associated with the strong lateral shear in the barotropic jet. Second, it is only over the last few years that computational resources reached a point where numerical models of the Southern Ocean can be run at sufficiently high horizontal resolution, such as the 1/20° horizontal grid spacing used here, to resolve jet dynamics in the Southern Ocean. Nevertheless, for the complete picture of Southern Ocean ventilation, one has to take into account both dynamics of the Southern Ocean MOC and jet dynamics; it is the delicate balance between these two processes that is relevant to understanding carbon and nutrient budgets in the past, current, and future Southern Ocean.

The model grid spacing used in this work is 1/20° in the horizontal, which resolves the jet dynamics presented here. This horizontal grid spacing needs to be compared to the 1° grid spacing (or coarser) used in studies that model past ocean circulation (due to their need to run over long time periods) and the 1/4° grid spacing of most climate models used by the Intergovernmental Panel on Climate Change (IPCC) to predict climate for the next centuries. A doubling of horizontal grid spacing, taking into account the necessary adjustments of the model time step, results in approximately an order of magnitude increase in computational resources. Extending this work to the global ocean to understand the impact of rapid changes in Southern Ocean ventilation on global climate would therefore push the current generation of supercomputers to their limits. Nevertheless,

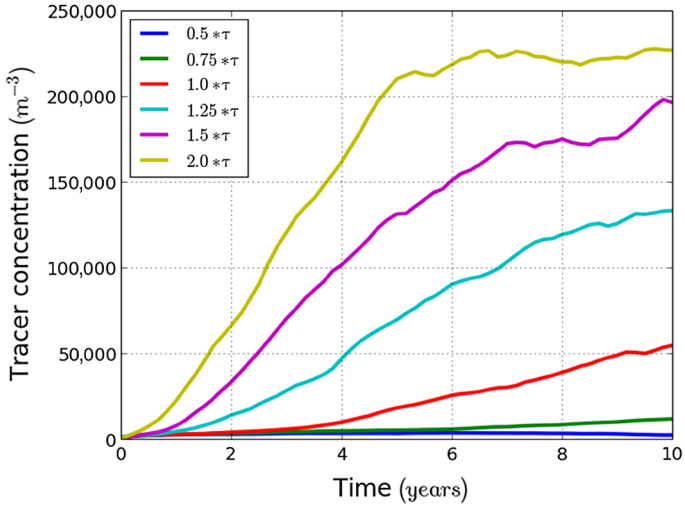

Fig. 9. Transients of tracer ventilation. Changes of tracer concentration integrated between depths of 500 and 1500 m with time. Colors represent the different wind perturbation experiments shown in Fig.1B.

with a steady increase in computational resources, it would be of great benefit to extend this work from being restricted to the Indian sector of the Southern Ocean to simulate the circumpolar Southern Ocean. In particular, Drake Passage is of great interest because of its central role in AAIW ventilation in our current climate. It is possible that a change in wind forcing in glacial climates could have resulted in a shutdown of Southern Ocean ventilation in this region, leading to the highly stratified Southern Ocean observed in glacial climates (*38*).

Reynolds stresses (convergence of eddy momentum fluxes) are crucial for maintaining Southern Ocean jets. Thus, to represent jet dynamics in simulations of past and future climates, it is necessary to either resolve or parameterize these Reynolds stresses. Both conceptual

models used to study the role of the global MOC and eddy parameterizations in more realistic models such as those used by the IPCC currently assume Reynolds stresses to be negligible. While regional models, such as the model used in this study, are capable of resolving Reynolds stresses using computational resources available today, it needs to be shown whether global climate simulations, run at lower grid spacing, are able to adequately represent these jet dynamics and associated changes in Southern Ocean ventilation. Until computational resources allow for global ocean models to fully resolve Reynolds stresses, these models rely on parameterizations of these unresolved processes. One approach to achieve this is to build on existing eddy parameterizations, which are limited to eddy buoyancy fluxes and include Reynolds stresses (*43*). Another promising approach is to parameterize Reynolds stresses using stochastic eddy parameterizations that improve jet dynamics in eddy-permitting ocean models, that is, models that partially resolve the relevant dynamics (*44*, *45*). Nevertheless, much work remains until these approaches can be applied in realistic simulations of global climate, with the abrupt change described in this study, at wind stresses predicted for the very near future, pointing toward the urgency to make progress in this field.

To develop adequate eddy parameterizations, it is first necessary to understand the underlying dynamics of the processes presented here. This study provides a very descriptive approach to show how jet dynamics can abruptly change, with important consequences for Southern Ocean ventilation, but many challenging questions about the detailed dynamics remain. While it has previously been demonstrated that jets can abruptly reorganize their structure as a consequence of small changes in their forcing (*30*), these efforts have been limited to highly idealized model configurations aimed at representing the atmospheres of Earth and giant gas planets, such as Jupiter and Saturn. Nevertheless, the abrupt change in jet dynamics presented here is closely related to the interaction of jets with topography and ocean stratification, both of which are absent in these previous studies. To explore the dynamics behind this abrupt jet reorganization, it is therefore necessary to work from the knowledge gained from these highly idealized model configurations toward the more complex dynamics described in this study.

The main caveats of this study are the very idealized surface forcing used and the regional, re-entrant domain of this model configuration. Here, the wind forcing is a zonal and annual mean, and it will have to be shown in future work how these results would change under a seasonal cycle or a large amount of stochastic variability on both seasonal and interannual time scales. Seasonal cycles and stochastic variability might also make it harder to detect the processes shown here. The passive tracer is also introduced at the ocean surface with a short time scale, which is equivalent to an infinite tracer reservoir in the SML, and it will have to be shown in future work how this choice affects the percentage change in ventilation presented here. While the processes described here could, to some extent, change in a more realistic model configuration with, for example, a global model domain and an interactive atmosphere, these caveats are also the strength of this particular model configuration. It is only in such an idealized model configuration that it is possible to separate the physical process of interest from many other processes occurring in a more complex model. Taking into account current limitations of supercomputing resources, it is also only possible to run multiple perturbation experiments with sufficient model grid spacing if the model domain is limited in its spatial extent. Several future directions to extend this work become apparent. The abrupt change in jet dynamics presented here leads to an abrupt increase in Rossby number, with consequences for submesoscale processes and hence the ventilation process. Submesoscale processes are barely resolved in this model configuration, and further work is necessary to understand changes in ventilation if these processes were resolved, including the interaction of submesoscale processes with the jet dynamics presented here. It also remains an open question why ventilation does not occur at the SEIR where a similar strong jet is observed. One difference in this region is that topography does not reach close to the surface, and the jet north of the SEIR is close to the boundary of the model domain, which could have effects on ventilation in this region. Another difference is that the jet in the SEIR moves in latitude with changes in wind stress, while the KP jet is pinned to its position by the KP. More idealized experiments would be necessary to understand this discrepancy. More work is also necessary to further understand the adjustment time scales of this abrupt change in jet dynamics and its role in Southern Ocean ventilation. The model results discussed here are based on equilibrated experiments, and hence, it is not known how long the wind has to increase for it to change Southern Ocean ventilation—is a storm enough, or an increase of winds during winter, or a long-term increase of winds as predicted by climate models for the coming decades? With more supercomputing resources becoming available in the future, much can be learned from using the idealized experiments used here in conjunction with more complex climate models to understand the consequences of jet dynamics on the global climate system.

MATERIALS AND METHODS

Ocean model configuration

The ocean model used was the Massachusetts Institute of Technology general circulation model (MITgcm) (*46*). It uses depth coordinates, partially filled cells for the bathymetry, a quadratic bottom drag coefficient of 0.0025, a nonlinear equation of state (*47*), a seventh-order advection scheme, and the K-profile parameterization (*48*). The model domain ranged from 57° to 129°E in longitude and 70° to 35°S in latitude and hence included the steep topography associated with the KP and the SEIR. The horizontal grid spacing was 1/20°, which converts to a zonal grid spacing of ~4.5 km at the northern boundary and ~1.9 km at the southern boundary, with a meridional grid spacing of ~5.6 km. The vertical resolution was resolved by 150 layers, ranging from 10 m thickness at the surface to 50 m thickness at depth.

The model topography was taken from the 1-min-resolution Shuttle Radar Topographic Mission (*49*) with a maximum depth of 5000 m. The model domain was made periodic in the east-west direction, and the topography was interpolated over 4° bands at its eastern and western bands to avoid discontinuities. The northern boundary was relaxed over a 1°-wide sponge layer with a relaxation time of 4 days to annually and zonally averaged climatological fields taken from year 2005 of the Southern Ocean State Estimate (*50*). At the ocean surface, the model was forced to the annually and zonally averaged sea-surface temperature (which was restored with a relaxation time of 15 days), freshwater fluxes, and wind forcing from the Southern Ocean State Estimate. The Southern Ocean MOC was calculated using the MITgcm's layer package (*51*), with the maximum value being determined for all regions south of the sponge layer. For this reference experiment, the total zonal transport was equal to 155 Sverdrup (1 Sverdrup = 10^6 m^3 s^{-1}), which was close to the observed value of the transport estimated in Drake Passage of 173.3 Sverdrup

(*52*). A more detailed comparison of this model configuration with observations can be found elsewhere (*53*, *54*).

Perturbation experiments

In the perturbation experiments, the westerly component of the wind stress was changed to multiples of the annually and zonally averaged wind stress of the year 2005 taken from the Southern Ocean State Estimate (Fig. 1B). With the 2005 winds used as the reference case, and denoted by τ, five perturbation experiments were run where the westerly component of the wind stress was perturbed to 0.5*τ, 0.75*τ, 1.25*τ, 1.5*τ, and 2*τ. In all perturbation experiments, forcing at the northern boundary and the surface remained the same as in the reference experiment. All perturbation experiments were run for 30 years starting from the equilibrated reference experiment, with results shown here being mean values over the last 10 years. Figure 8 shows EKE, baroclinic transports (T_{bci}), barotropic transports (T_{btp}), and maximum Southern Ocean MOC (Ψ_{max}) for all perturbation experiments. Similar to EKE derived from satellite observations and modeling studies, EKE increases with increasing wind forcing (*55*, *56*). Because of the complex topography in the model, baroclinic and barotropic transports were calculated using a two-layer model approximation (*57*) at the most eastern longitude of the model domain. The barotropic transport (T_{btp}) was defined as the average velocity in the bottom layer multiplied by the ocean depth, and the baroclinic transport (T_{bci}) was defined as the difference in transport between the upper and lower layers. The boundary between the two layers was chosen to be 1600 m, with the transport anomalies in the perturbation experiments being insensitive to this choice (*57*). As shown in Fig. 8, the baroclinic transport changed very little with wind stress, an effect known as "eddy saturation" (*56*, *58*), whereas the barotropic transport increased with wind stress. The insensitivity of the baroclinic transport is the reason why ocean observations show little change in isopycnal slopes over recent decades during which wind speeds increased (*59*). The Southern Ocean MOC increases less than linearly with wind stress owing to a partial compensation of the wind stress by mesoscale eddies, an effect known as "eddy compensation" (*2*). All of these metrics agree with previous work.

Tracer ventilation

A passive tracer has been introduced at the ocean surface over the last 10 years of model integration. This is done by relaxing the tracer concentration to a value of 1, with a relaxation time scale of 2 hours, homogeneously everywhere south of 37.6°S. North of this latitude, no tracer is introduced because of the numerics of the sponge layer, leading to unphysical vertical motion of the tracer. At the northern boundary of the model domain, the tracer concentration is relaxed to zero to simulate the tracer leaving the domain. The transient increase in tracer concentration in the mid-depth Southern Ocean, integrated between depths of 500 and 1500 m, is shown in Fig. 9. Tracer concentrations increase over approximately 5 years before leveling off due to the tracer being relaxed to zero once reaching the northern sponge layer. Tracer concentrations shown in Fig. 4 are a 2-month mean after 5 years of tracer input at the ocean surface.

REFERENCES AND NOTES

1. W. S. Broecker, Glacial to interglacial changes in ocean chemistry. *Prog. Oceanogr.* **11**, 151–197 (1982).
2. J. L. Sarmiento, J. R. Toggweiler, A new model for the role of the oceans in determining atmospheric PCO_2. *Nature* **308**, 621–624 (1984).
3. D. M. Sigman, M. P. Hain, G. H. Haug, The polar ocean and glacial cycles in atmospheric CO_2 concentration. *Nature* **466**, 47–55 (2010).
4. J. Gottschalk, L. C. Skinner, J. Lippold, H. Vogel, N. Frank, S. L. Jaccard, C. Waelbroeck, Biological and physical controls in the Southern Ocean on past millennial-scale atmospheric CO_2 changes. *Nat. Commun.* **7**, 11539 (2016).
5. A. C. Naveira Garabato, L. Jullion, D. P. Stevens, K. J. Heywood, B. A. King, Variability of Subantarctic Mode Water and Antarctic Intermediate Water in the Drake Passage during the late-twentieth and early-twenty-first centuries. *J. Climate* **22**, 3661–3688 (2009).
6. W. J. Schmitz Jr., On the interbasin-scale thermohaline circulation. *Rev. Geophys.* **33**, 151–173 (1995).
7. L. D. Talley, Freshwater transport estimates and the global overturning circulation: Shallow, deep and throughflow components. *Prog. Oceanogr.* **78**, 257–303 (2008).
8. C. L. Sabine, R. A. Feely, N. Gruber, R. M. Key, K. Lee, J. L. Bullister, R. Wanninkhof, C. S. Wong, D. W. R. Wallace, B. Tilbrook, F. J. Millero, T.-H. Peng, A. Kozyr, T. Ono, A. F. Rios, The oceanic sink for anthropogenic CO_2. *Science* **305**, 367–371 (2004).
9. K. Pahnke, S. L. Goldstein, S. R. Hemming, Abrupt changes in Antarctic intermediate water circulation over the past 25,000 years. *Nat. Geosci.* **1**, 870–874 (2008).
10. K. Pahnke, R. Zahn, Southern Hemisphere water mass conversion linked with North Atlantic Climate variability. *Science* **307**, 1741–1746 (2005).
11. O. A. Saenko, A. J. Weaver, J. M. Gregory, On the link between the two modes of the ocean thermohaline circulation and the formation of global-scale water masses. *J. Climate* **16**, 2797–2801 (2003).
12. R. J. Stouffer, D. Seidov, B. J. Haupt, Climate response to external sources of freshwater: North Atlantic versus the Southern Ocean. *J. Climate* **20**, 436–448 (2007).
13. J. Marshall, K. Speer, Closure of the meridional overturning circulation through Southern Ocean upwelling. *Nat. Geosci.* **5**, 171–180 (2012).
14. A. K. Morrison, T. L. Frölicher, J. L. Sarmiento, Upwelling in the Southern Ocean. *Phys. Today* **68**, 27 (2015).
15. J. M. Lauderdale, R. G. Williams, D. R. Munday, D. P. Marshall, The impact of Southern Ocean residual upwelling on atmospheric CO_2 on centennial and millennial timescales. *Clim. Dyn.* **48**, 1611–1631 (2017).
16. T. DeVries, M. Holzer, F. Primeau, Recent increase in oceanic carbon uptake driven by weaker upper-ocean overturning. *Nature* **542**, 215–218 (2017).
17. U. Siegenthaler, Th. Wenk, Rapid atmospheric CO_2 variations and ocean circulation. *Nature* **308**, 624–626 (1984).
18. J. Viehbahn, C. Eden, Towards the impact of eddies on the response of the Southern Ocean to climate change. *Ocean Model.* **34**, 150–165 (2010).
19. R. F. Anderson, S. Ali, L. I. Bradtmiller, S. H. H. Nielsen, M. Q. Fleisher, B. E. Anderson, L. H. Burckle, Wind-driven upwelling in the southern ocean and the deglacial rise in atmospheric CO_2. *Science* **323**, 1443–1448 (2009).
20. A. J. Watson, G. K. Vallis, M. Nikurashin, Southern Ocean buoyancy forcing of ocean ventilation and glacial atmospheric CO_2. *Nat. Geosci.* **8**, 861–864 (2015).
21. R. Ferrari, M. F. Jansen, J. F. Adkins, A. Burke, A. L. Stewart, A. F. Thompson, Antarctic sea ice control on ocean circulation in present and glacial climates. *Proc. Natl. Acad. Sci. U.S.A.* **111**, 8753–8758 (2014).
22. J. Viebahn, C. Eden, Towards the impact of eddies on the response of the Southern Ocean to climate change. *Ocean Model.* **34**, 150–165 (2010).
23. N. C. Swart, J. C. Fyfe, Observed and simulated changes in the Southern Hemisphere surface westerly wind-stress. *Geophys. Res. Lett.* **39**, L16711 (2012).
24. C. Le Quéré, C. Rödenbeck, E. T. Buitenhuis, T. J. Conway, R. Langenfelds, A. Gomez, C. Labuschagne, M. Ramonet, T. Nakazawa, N. Metzl, N. Gillett, M. Heimann, Saturation of the Southern Ocean CO_2 sink due to recent climate change. *Science* **316**, 1735–1738 (2007).
25. K Zickfeld, J. C. Fyfe, M. Eby, A. J. Weaver, Comment on "Saturation of the Southern Ocean CO_2 sink due to recent climate change". *Science* **319**, 570 (2008).
26. H. C. Bostock, P. J. Sutton, M. J. M. Williams, B. N. Opdyke, Reviewing the circulation and mixing of Antarctic Intermediate Water in the South Pacific using evidence from geochemical tracers and Argo float trajectories. *Deep Sea Res. I* **73**, 84–98 (2013).
27. R. G. Williams, C. Wilson, C. W. Hughes, Ocean and atmosphere storm tracks: The role of eddy vorticity forcing. *J. Phys. Oceanogr.* **37**, 2267–2289 (2007).
28. K. R. Hendry, L. F. Robinson, M. P. Meredith, S. Mulitza, C. M. Chiessi, H. Arz, Abrupt changes in high-latitude nutrient supply to the Atlantic during the last glacial cycle. *Geology* **40**, 123–126 (2012).
29. H.-I. Kuo, Dynamic instability of two-dimensional nondivergent flow in a barotropic atmosphere. *J. Meteor.* **6**, 105–122 (1949).
30. B. F. Farrell, P. J. Ioannou, Formation of jets by baroclinic turbulence. *J. Atmos. Sci.* **65**, 3353–3375 (2008).
31. I. N. James, Suppression of baroclinic instability in horizontally sheared flows. *J. Atmos. Sci.* **44**, 3710–3720 (1987).
32. L. N. Thomas, R. Ferrari, Friction, frontogenesis, and the stratification of the surface mixed layer. *J. Phys. Oceanogr.* **38**, 2501–2518 (2008).

33. A. Mahadevan, The impact of submesoscale physics on primary productivity of plankton. *Ann. Rev. Mar. Sci.* **8**, 161–184 (2016).
34. J.-B. Sallée, K. Speer, S. Rintoul, S. Wijffels, Southern ocean thermocline ventilation. *J. Phys. Oceanogr.* **40**, 509–529 (2010).
35. J.-B. Sallée, R. J. Matear, S. R. Rintoul, A. Lenton, Localized subduction of anthropogenic carbon dioxide in the Southern Hemisphere oceans. *Nat. Geosci.* **5**, 579–584 (2012).
36. J. Llort, C. Langlais, R. Matear, S. Moreau, A. Lenton, P. G. Strutton, Evaluating southern ocean carbon eddy-pump from biogeochemical-argo floats. *J. Geophys. Res. Oceans* **123**, 971–984 (2018).
37. A. Foppert, K. A. Donohue, D. R. Watts, The polar front in Drake passage: A composite-mean stream-coordinate view. *J. Geophys. Res. Oceans* **121**, 1771–1788 (2016).
38. R. Franois, M. A. Altabet, E.-F. Yu, D. M. Sigman, M. P. Bacon, M. Frank, G. Bohrmann, G. Bareille, L. D. Labeyrie, Contribution of Southern Ocean surface-water stratification to low atmospheric CO_2 concentrations during the last glacial period. *Nature* **389**, 929–935 (1997).
39. K.-F. Huang, D. W. Oppo, W. B. Curry, Decreased influence of Antarctic intermediate water in the tropical Atlantic during North Atlantic cold events. *Earth Planet. Sci. Lett.* **389**, 200–208 (2014).
40. S. Sun, I. Eisenman, A. L. Stewart, The influence of Southern Ocean surface buoyancy forcing on glacial-interglacial changes in the global deep ocean stratification. *Geophys. Res. Lett.* **43**, 8124–8132 (2016).
41. J. F. Adkins, The role of deep ocean circulation in setting glacial climates. *Paleoceanography* **28**, 539–561 (2013).
42. A. F. Thompson, A. C. Naveira Garabato, Equilibration of the Antarctic Circumpolar Current by standing meanders. *J. Phys. Oceanogr.* **44**, 1811–1828 (2014).
43. D. P. Marshall, J. R. Maddison, P. S. Berloff, A framework for parameterizing eddy potential vorticity fluxes. *J. Phys. Oceanogr.* **42**, 539–557 (2012).
44. L. Zanna, P. G. L. Porta Mana, J. Anstey, T. David, T. Bolton, Scale-aware deterministic and stochastic parameterizations of eddy-mean flow interaction. *Ocean Model.* **111**, 66–80 (2017).
45. J. A. Anstey, L. Zanna, A deformation-based parameterization of ocean mesoscale eddy Reynolds stresses. *Ocean Modell.* **112**, 99–111 (2017).
46. J. Marshall, A. Adcroft, C. Hill, L. Perelman, C. Heisey, A finite-volume, incompressible Navier Stokes model for studies of the ocean on parallel computers. *J. Geophys. Res.* **102**, 5753–5766 (1997).
47. D. R. Jackett, T. J. McDougall, Minimal adjustment of hydrographic profiles to achieve static stability. *J. Atmos. Oceanic Tech.* **12**, 381–389 (1995).
48. W. G. Large, J. C. McWilliams, S. C. Doney, Oceanic vertical mixing: A review and a model with nonlocal boundary layer parameterization. *Rev. Geophys.* **32**, 363–403 (1994).
49. W. H. F. Smith, D. T. Sandwell, Global sea floor topography from satellite altimetry and ship depth soundings. *Science* **277**, 1956–1962 (1997).
50. M. R. Mazloff, P. Heimbach, C. Wunsch, An eddy-permitting Southern Ocean state estimate. *J. Phys. Oceanogr.* **40**, 880–899 (2010).
51. R. Abernathey, J. Marshall, D. Ferreira, The dependence of Southern Ocean meridional overturning on wind stress. *J. Phys. Oceanogr.* **41**, 2261–2278 (2011).
52. K. A. Donohue, K. L. Tracey, D. R. Watts, M. P. Chidichimo, T. K. Chereskin, Mean Antarctic Circumpolar Current transport measured in Drake Passage. *Geophys. Res. Lett.* **43**, 11760–11767 (2016).
53. I. Rosso, A. McC. Hogg, P. G. Strutton, A. E. Kiss, R. Matear, A. Klocker, E. van Sebille, Vertical transport in the ocean due to sub-mesoscale structures: Impacts in the Kerguelen region. *Ocean Model.* **80**, 10–23 (2014).
54. I. Rosso, A. McC. Hogg, A. E. Kiss, B. Gayen, Topographic influence on submesoscale dynamics in the Southern Ocean. *Geophys. Res. Lett.* **42**, 1139–1147 (2015).
55. A. McC. Hogg, M. P. Meredith, D. P. Chambers, E. P. Abrahamsen, C. W. Hughes, A. K. Morrison, Recent trends in the Southern Ocean eddy field. *J. Geophys. Res.* **120**, 257–267 (2015).
56. D. R. Munday, H. L. Johnson, D. P. Marshall, Eddy saturation of equilibrated circumpolar currents. *J. Phys. Oceanogr.* **43**, 507–532 (2013).
57. C. E. Langlais, S. R. Rintoul, J. D. Zika, Sensitivity of Antarctic circumpolar current transport and eddy activity to wind patterns in the Southern Ocean. *J. Phys. Oceanogr.* **45**, 1051–1067 (2015).
58. D. N. Straub, On the transport and angular momentum balance of channel models of the Antarctic Circumpolar Current. *J. Phys. Oceanogr.* **23**, 776–782 (1993).
59. C. W. Böning, A. Dispert, M. Visbeck, S. R. Rintoul, F. U. Schwarzkopf, The response of the Antarctic Circumpolar Current to recent climate change. *Nat. Geosci.* **1**, 864–869 (2008).

Acknowledgments: I want to thank L. Zanna, D. R. Munday, D. P. Marshall, and C. Langlais for useful discussions that helped to improve this manuscript. I also want to thank the three anonymous reviewers for very constructive comments that helped to substantially improve this manuscript. **Funding:** A.K. was supported by an Australian Research Council Discovery Early Career Researcher Award (DE140100076). This research was undertaken with the assistance of resources from the National Computational Infrastructure, which is supported by the Australian Government. **Author contributions:** A.K. developed the model configuration, concept, and wrote the manuscript. **Competing interests:** The author declares that he has no competing interests. **Data and materials availability:** All data needed to evaluate the conclusions in the paper are present in the paper. The numerical ocean model is available at http://mitgcm.org/. Additional data related to this paper may be requested from the author.

Submitted 24 July 2017
Accepted 2 August 2018
Published 3 October 2018
10.1126/sciadv.aao4719

Citation: A. Klocker, Opening the window to the Southern Ocean: The role of jet dynamics. *Sci. Adv.* **4**, eaao4719 (2018).

ScienceAdvances

Opening the window to the Southern Ocean: The role of jet dynamics

Andreas Klocker

Sci Adv **4** (10), eaao4719.
DOI: 10.1126/sciadv.aao4719

Science Advances (ISSN 2375-2548) is published by the American Association for the Advancement of Science, 1200 New York Avenue NW, Washington, DC 20005.